



**HAL**  
open science

# Estimating the properties of bone phantom cylinders through the inversion of axially transmitted low-frequency ultrasonic guided waves

Aubin Chaboty, Vu-Hieu Nguyen, Guillaume Haiat, Pierre Bélanger

## ► To cite this version:

Aubin Chaboty, Vu-Hieu Nguyen, Guillaume Haiat, Pierre Bélanger. Estimating the properties of bone phantom cylinders through the inversion of axially transmitted low-frequency ultrasonic guided waves. *Ultrasonics*, 2025, 155, pp.107694. <10.1016/j.ultras.2025.107694>. <hal-05352717>

**HAL Id: hal-05352717**

**<https://hal.science/hal-05352717v1>**

Submitted on 7 Nov 2025

HAL is a multi-disciplinary open access archive for the deposit and dissemination of scientific research documents, whether they are published or not. The documents may come from teaching and research institutions in France or abroad, or from public or private research centers.

L'archive ouverte pluridisciplinaire HAL, est destinée au dépôt et à la diffusion de documents scientifiques de niveau recherche, publiés ou non, émanant des établissements d'enseignement et de recherche français ou étrangers, des laboratoires publics ou privés.



HAL Authorization

## Highlights

### **Estimating the properties of bone phantom cylinders through the inversion of axially transmitted low-frequency ultrasonic guided waves**

Aubin Chaboty, Vu-Hieu Nguyen, Guillaume Haiat, Pierre Bélanger

- Assessment of bone phantom properties using low-frequency (under 500 kHz) ultrasonic guided waves.
- Implementation of SAIGA-based inversion method.
- Inversion algorithm focused on high amplitude modes.
- Accurate estimation of bone phantom properties in scenario simulating *in-vivo* conditions.

# Estimating the properties of bone phantom cylinders through the inversion of axially transmitted low-frequency ultrasonic guided waves

Aubin Chaboty<sup>a,1</sup>, Vu-Hieu Nguyen<sup>b</sup>, Guillaume Haiat<sup>c</sup>, Pierre Bélanger<sup>a</sup>

<sup>a</sup>*PULETS, École de Technologie Supérieure, Montréal, H3C 1K3, Québec, Canada*

<sup>b</sup>*MSME, CNRS, UMR 8208, Université Paris Est Créteil, Université Gustave Eiffel, F-94010 Créteil, France*

<sup>c</sup>*MSME, CNRS, UMR 8208, F-94010 Créteil, France*

---

## Abstract

Early detection of osteoporosis has increasingly focused on ultrasonic methods, particularly guided waves in axial transmission to assess cortical bone properties. This study demonstrates the potential of low-frequency measurements (<500 kHz) for accurately inferring cortical mechanical and geometrical properties. A custom ultrasonic transducer centered at 350 kHz was used to acquire data, processed via a 2D fast Fourier transform to obtain dispersion curves. These were compared with simulations generated using the semi-analytical iso-geometric analysis (SAIGA) method, modeling a quasi-cylindrical bone geometry in void or immersed in olive oil. By incorporating an excitability parameter into the inversion algorithm, the proposed method achieved a less than 5% discrepancy between bone phantom properties determined via SAIGA inversion and bulk wave pulse-echo measurements, demonstrating its accuracy and potential for in vivo applications.

---

<sup>1</sup>aubin.chaboty.1@ens.etsmtl.ca

Results also showed that high-wavenumber modes predominantly reflect material properties, whereas low-wavenumber modes below 100 kHz are sensitive to the overall bone geometry, highlighting the importance of low frequencies for a global bone characterization.

*Keywords:* Axial transmission, low-frequency ultrasonic guided waves, cortical bone, SAIGA method, inversion algorithm

---

## 1. Introduction

Osteoporosis is a bone disease characterized by a reduction in bone strength which increases the risk of fracture [1, 2]. Early identification is essential, as it facilitates prompt treatment and fracture prevention. Bone mineral density (BMD) assessment using dual-X-ray absorptiometry (DEXA) has been used as the gold standard for the diagnostics of this pathology. However, BMD alone is not sufficient to assess the risk of fracture [3], and often family history is a more reliable method [4]. A thorough assessment of an individual's bone quality should take into account additional factors, including bone rigidity, cortical thickness, and bone volume fraction [3, 5].

Quantitative ultrasound (QUS) techniques have emerged as noninvasive and nonionizing methods in various biomedical applications. This technique is particularly well-suited for evaluating bone quality by measuring ultrasonic wave speed and attenuation [6, 7]. Moreover, QUS methods are easy to use and not expensive, which may facilitate the monitoring of the disease.

The use of ultrasonic guided waves is a popular technique employed in nondestructive testing, particularly for analyzing and characterizing materials such as composite or bonded plates [8]. In recent years, this technique has

19 been adapted for examining long cortical bone such as the tibia, radius, and  
20 femur [9, 10]. Early research on axial propagation mainly concentrated on  
21 determining the time-of-flight (TOF) of the earliest detected signal, known  
22 as the first-arriving signal (FAS). Subsequently, the speed of the quickest  
23 waveform was determined and often linked to the fundamental symmetric  
24 mode of a plate [11, 12]. Several clinical studies have shown that the FAS ve-  
25 locity can be used to differentiate between healthy individuals and those with  
26 osteoporosis [13, 14]. Another way to use axial transmission technique is to  
27 focus on the dispersive trajectories of the mode propagating in the waveguide.  
28 However, these methods involve solving a complex multi-parameter problem  
29 to access the mechanical and geometrical properties of the bone [15, 16]. In-  
30 version algorithms or deep learning analysis can be used in an attempt to  
31 match experimental and simulated data. In this context, two approaches can  
32 be distinguished: using a simplified model at high frequencies ( $> 1$  MHz),  
33 due to high attenuation and limited penetration depth [17], or using a bone  
34 representative model at lower frequencies ( $< 500$  kHz), which allows for the  
35 estimation of the overall geometry.

36 At high frequencies, ultrasonic guided waves exhibit a reduced depth of  
37 penetration within the medium [17], enabling the approximation of long bone  
38 to a plate-like structure. This approximation facilitates the analysis and in-  
39 terpretation of wave propagation by treating the cortical layer as a thin  
40 plate, reducing the model's complexity. Due to the large number of modes  
41 propagating at these frequencies, several parameters of the bone cortex can  
42 be retrieved through inversion analysis. Foiret et al. [18] proposed an in-  
43 verse characterization technique to determine the thickness and bulk wave

44 velocities of *ex vivo* cortical bone samples, utilizing a transversely isotropic  
45 free plate model integrated with a parameter-sensitive algorithm. Following  
46 this, the same group applied genetic algorithm-based inversion schemes to  
47 interpret multimodal datasets, circumventing the need for prior assumptions  
48 about mode order [19]. However, the presence of soft tissues in the model  
49 adds a significant number of modes and a greater attenuation [20], increas-  
50 ing its complexity when extracting dispersion curves [21, 22]. Deep neural  
51 networks were introduced as an alternative to inversion algorithms. They  
52 overcome the complexity introduced by the bi-layer model, providing better  
53 estimates of cortical thickness and properties [23]. While the bone can be  
54 approximated as a plate at high frequencies and so simplifying the model,  
55 the important number of propagating modes makes the inverse problem a  
56 complex endeavor. Additionally, a plate model fails to capture the overall  
57 shape of the bone, which is crucial for assessing its structural strength.

58 Using low frequencies allows the wave to penetrate deeper into the bone  
59 cortex, enabling a comprehensive assessment of its entire cross-section. This  
60 characteristic makes the use of guided waves at low frequencies particularly  
61 useful for diagnosing osteoporosis, which primarily affects the inner part of  
62 the structure [24]. However, due to a lower number of modes propagating  
63 at low frequencies, less information and bone parameters are likely to be  
64 obtained through the axial propagation of guided waves. Previous studies  
65 have shown the capability of low-frequency ultrasonic guided waves to esti-  
66 mate the cortical thickness of free isotropic plates, which was later applied to  
67 tubular structure and *ex-vivo* bones [25]. Likewise, another research group  
68 employed a hollow isotropic cylinder filled with a viscous liquid to assess the

69 thickness of bovine tibia specimens by manually correlating experimental ve-  
70 locities with the phase velocities of simulated modes [26]. Peirera *et al.* [15]  
71 have shown that very low frequencies (under 60 kHz) can accurately retrieve  
72 the shape of cadaveric radius specimens by using mode amplitudes in the  
73 dispersion curves. Using this principle of amplitude, Chaboty *et al.* further  
74 demonstrated the capability of low-frequency axial transmission technique  
75 (under 500 kHz) to precisely measure the thickness and velocities of a bi-layer  
76 bone phantom plate with an overlaying soft tissue layer [27]. The dispersive  
77 properties of ultrasonic guided wave modes combined with the mode am-  
78 plitude can compensate for the lack of information encountered when using  
79 low-frequencies, providing an accurate estimation of the bone health.

80 This paper demonstrates the potential of low-frequency ultrasonic guided  
81 waves (50–500 kHz) to retrieve the cortical mechanical properties and geome-  
82 try of a quasi-cylindrical phantom filled with soft tissue. The frequency range  
83 enables the determination of velocity parameters and geometrical properties,  
84 while the excitability of propagating modes enhances the inversion accu-  
85 racy. Using the semi-analytical iso-geometric analysis (SAIGA) method, a  
86 parameterized cortical bone cylinder was simulated to estimate experimental  
87 bone phantom properties. Dispersion curves, derived from 2D fast Fourier  
88 transform processing of measurements made with a proprietary transducer,  
89 were compared with semi-analytical predictions. The inversion algorithm  
90 estimated five parameters: longitudinal and shear wave velocities, cortical  
91 thickness, mean radius, and density. The manuscript is organized as follows:  
92 Section 2 outlines the model, inversion algorithm, and experimental proto-  
93 cols; Section 3 present the sensitivity analysis, dispersion curve fitting, and

94 property estimations; Section 4 interprets the findings, and finally the Con-  
95 clusion summarizes the study's contributions to ultrasonic guided wave-based  
96 bone characterization.

## 97 **2. Material and Methods**

### 98 *2.1. Models and simulations models*

99 A model consisting of a bone phantom cylinder filled with soft tissue,  
100 representative of the experimental bone phantom cylinders, was employed  
101 for the inversion of experimental dispersion curves. An outer layer of viscous  
102 fluid was added to the model to reflect the immersed case. Section 2.1.1 out-  
103 lines the cylindrical model for the forward simulation in this study. Section  
104 2.1.2 subsequently provides an overview of the SAIGA method for solving  
105 the forward problem and details the formulation of the mode excitability  
106 employed [28, 29].

#### 107 *2.1.1. Numerical model*

108 The model was based on the experimental bone phantom cylinders and  
109 assumes a homogeneous, isotropic, cylinder-like structure ( $\Omega^S$ ) of infinite  
110 length and constant cross-section of thickness  $h^S$  and outer radius  $r^S$  along  
111 the direction of propagation ( $e_3$ ). While it does not represent a perfect cylin-  
112 der to account for the asymmetry of the experimental phantoms, the term  
113 "cylinder" will be used throughout the text for the sake of simplicity. This  
114 simulated cylinder is filled with soft tissue material ( $\Omega^{fi}$ ). In the second part  
115 of the study (Section 3.3.2), this cylinder is then embedded in a viscous fluid  
116 ( $\Omega^{fo}$ ) of minimum thickness  $h^{fo}$ , square-shaped to reflect the experimental

117 container. Fig. 1 shows a description of the model geometry as well as a  
118 photograph of both cylinder phantoms and their cross-section. As it can be  
119 seen on Fig. 1(c), phantom cylinders are not perfectly cylindrical with some  
120 irregularities in their cross section. Unlike an ideal cylinder, the osteoporotic  
121 phantom has a radius ratio ( $max(r^S)/min(r^S)$  along the axis of the bone  
122 phantom) of 1.106, compared to 1.097 for the healthy bone phantom.

123 The phantom models only represented the cross-section, with the wave  
124 assumed to propagate harmonically along the bone axis (refer to 2.1.2 in the  
125 SAIGA method). Consequently, throughout this manuscript, we will refer  
126 to this model type as a "2.5D model." In general, 2.5D modeling applies to  
127 cases that are two-dimensional in one plane (here, the  $(e_1)$  and  $(e_2)$  axes)  
128 but exhibit some level of variation or complexity in the third dimension  
129 (typically the  $(e_3)$  axis). This third dimension is often treated in a simplified  
130 or approximate way, often by making assumptions regarding its behavior [30,  
131 29]. For example, in the context of guided wave propagation in a cylindrical  
132 structure, a 2.5D model represents the cross-section of the cylinder in the  $(e_1-$   
133  $e_2)$  plane, while the axial direction  $(e_3)$  is modeled using an exponential term  
134 function of the wavenumber in the wave propagation direction:  $\exp[i(k_3x_3 -$   
135  $\omega t)]$  in eq.3. This approach allows capturing the essential physics of the  
136 problem while reducing computational complexity compared to a full 3D  
137 model.

138 The cortical layer of the model was defined as homogeneous and viscoelas-  
139 tic with a density  $(\rho)$ , and longitudinal  $(c_P)$  and shear  $(c_S)$  wave velocities.  
140 Two attenuation coefficients  $\alpha_P$  and  $\alpha_S$  of longitudinal and shear waves re-  
141 spectively were added to the model for defining the viscoelastic tensor. A

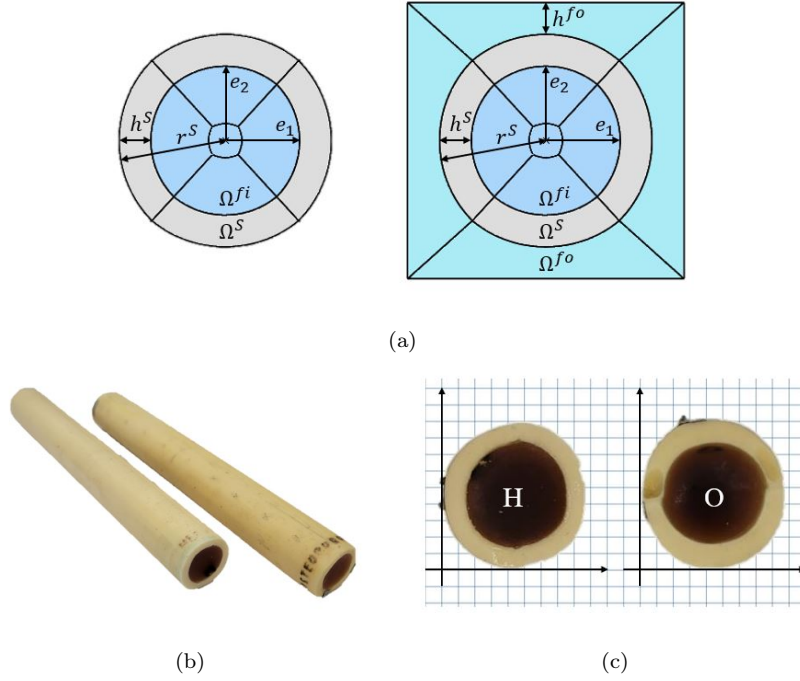


Figure 1: (a) Geometrical description of the numerical model with and without the outer fluid domain. (b) Experimental bone phantom cylinders measuring 150 mm in length. (c) Cross section of the healthy «H» and osteoporotic «O» bone phantoms.

142 ratio  $\alpha_P/\alpha_S$  at 1 MHz was fixed at 1.5 [31, 32], with  $\alpha_P = 2.9$  dB/cm at this  
 143 frequency, in accordance with the manufacturer properties. The viscosity  
 144 coefficients were calculated as [20, 33]:

$$\begin{cases} \eta_{11} = \frac{\alpha_P}{8.686} \times 2c_P \times \frac{C_{11}}{(\omega_{ref})^2} \\ \eta_{66} = \frac{\alpha_S}{8.686} \times 2c_S \times \frac{C_{66}}{(\omega_{ref})^2} \\ \eta_{13} = \eta_{11} - 2 \times \eta_{66} \end{cases} \quad (1)$$

145 where  $\omega_{ref} = 2\pi f_{req}$  with  $f_{req} = 1$  MHz the reference frequency used for the  
 146 calculation of the viscosity tensor. The values of  $\eta_{11}$ ,  $\eta_{13}$ , and  $\eta_{66}$  are kept

147 constant within the frequency bandwidth of interest and determined by the  
 148 value of the attenuation coefficients at frequency  $f_{req}$ . The complex elasticity  
 149 tensor is then expressed as  $C^* = C + i\eta\omega_{ref}$ .

150 The inner and outer layers were modeled as linear acoustic fluids of density  
 151 ( $\rho^{fi}$ ) and ( $\rho^{fo}$ ) respectively, with their corresponding wave velocities ( $c_P^{fi}$ )  
 152 and ( $c_P^{fo}$ ). As the phantoms were provided by the same manufacturer as the  
 153 plates used in Chaboty *et al.* [27], the properties of the inner soft tissue  
 154 were assumed to be the same as the properties of the soft tissue layer used  
 155 in [27]. Therefore  $\rho^{fi} = 977 \text{ kg/m}^3$  and  $c_P^{fi} = 1390 \text{ m/s}$ , with an attenuation  
 156 coefficient  $\alpha^{fi} = 0.6 \text{ dB/cm}$  at 1 MHz. For the outer layer, olive oil was  
 157 used as viscous fluid for experiments. This choice was made to provide a  
 158 greater attenuation in comparison with water, while keeping the celerity and  
 159 the density close to those of soft tissue [34]. As a result, the outer layer's  
 160 properties were defined with a density of  $\rho^{fo} = 913 \text{ kg/m}^3$ , a speed of sound  
 161 of  $c_P^{fo} = 1455 \text{ m/s}$ , and an attenuation of  $\alpha^{fo} = 0.05 \text{ dB/cm}$  at 1 MHz  
 162 [35, 36, 37]. The viscoelastic coefficient of both fluids was calculated as  
 163 follows :

$$\begin{cases} \eta^{f(i,o)} = \frac{\alpha^{f(i,o)}}{8.686} \times 2c_P^{f(i,o)} \times \frac{K^{f(i,o)}}{(\omega_{ref})^2} \\ K^{f(i,o)} = \rho^{f(i,o)} \left(c_P^{f(i,o)}\right)^2 \end{cases} \quad (2)$$

### 164 2.1.2. SAIGA method and excitability formulation

165 Based on the principles of the semi-analytical finite element method  
 166 (SAFE) [30, 38, 39], the SAIGA method is used to compute simulated dis-  
 167 persion curves. The method assumes harmonic wave propagation along the  
 168 propagation direction ( $e_3$ ), which corresponds to the cylinder's axial direc-  
 169 tion. The displacement field  $\mathbf{u}$  for the solid layer and pressure field in inner

170 and outer fluids  $\mathbf{p}_{i,o}$  can be expressed as:

$$\begin{cases} \mathbf{u}(x_1, x_2, x_3, t) = \mathbf{U}(x_1, x_2) \exp[i(k_3 x_3 - \omega t)] \\ \mathbf{p}_{i,o}(x_1, x_2, x_3, t) = \mathbf{P}_{i,o}(x_1, x_2) \exp[i(k_3 x_3 - \omega t)] \end{cases} \quad (3)$$

171 where  $i^2 = -1$ ;  $\omega \in \mathbb{R}$  is the angular frequency;  $k_3$  is the wavenumber in  
 172 the direction of propagation ( $e_3$ ); the vector  $\mathbf{U}(x_1, x_2) = (U_1, U_2, U_3)^T$  and  
 173  $\mathbf{P}_{i,o}(x_1, x_2) = P_{i,o}$  are the amplitudes of the displacement vector in  $(\Omega^S)$  and  
 174 of the pressures in  $(\Omega^{f(i,o)})$ , respectively. The use of the SAIGA method  
 175 results in a quadratic eigenvalue problem that must be solved to determine  
 176 the relationship between the wavenumber  $k_3$  and the angular frequency  $\omega$ .  
 177 This relationship can be obtained with respect to  $k_3$  as follows:

$$(-\omega^2 \mathbf{M} + \mathbf{K}_0 + ik_3 \mathbf{K}_1 + k_3^2 \mathbf{K}_2) \mathbf{V} = \mathbf{0} \quad (4)$$

178 where  $\mathbf{V} = (\mathbf{P}, \mathbf{U})^T$  denotes the global eigenvector, comprising the pressure  
 179 eigenvector ( $\mathbf{P}$ ) and the displacement eigenvector ( $\mathbf{U}$ ), while  $\mathbf{M}, \mathbf{K}_0, \mathbf{K}_1, \mathbf{K}_2$   
 180 represent the global matrices of the system and are not dependent on  $k_3$ . The  
 181 global matrix formulation was detailed by Seyfaddini *et al.* [29, 28]. For every  
 182 instance of the angular frequency  $\omega$ , solving Eq.(4) yields the eigenvalues  
 183  $k_3$ , along with their corresponding eigenvectors denoted as  $\mathbf{V}(\omega, k_3)$ . These  
 184 values represent the characteristics of the guided modes. Additionally, the  
 185 frequency-dependent phase velocity ( $c_{ph}$ ) and attenuation ( $att$ ) of a particular  
 186 guided mode can be calculated using these parameters.

$$c_{ph} = \omega / \Re(k_3) \text{ m/s} \quad att(\omega) = \Im(k_3) \text{ Np/m} \quad (5)$$

187 NURBS basis functions of order 3 were used for SAIGA analysis. The  
 188 model was divided into 4 patches as shown in Fig. 1(a). Every patch was

189 then divided to ensure acceptable precision in the calculation of dispersion  
 190 curves. Therefore, the number of degrees of freedom for the model accounts  
 191 for  $N_{Dof} = 361$ . The dispersion curves were calculated over a frequency  
 192 range spanning from 50 kHz to 500 kHz, in increments of 5 kHz.

193 To ensure that the inversion of the experimental dispersion curves was  
 194 targeting the most significant modes, the excitability  $Ex$  for a specific mode  
 195 was calculated according to its mode shape. Using the same formulation as  
 196 presented in Chaboty *et al.* [27] and based on previous works [40, 15], the  
 197 excitability value can be formulated in cylindrical coordinates as:

$$\begin{cases} Ex(k_3, \omega) = \frac{\Re(k_3, \omega)}{\Im(k_3, \omega)} \times U_{norm}^2(k_3, \omega) \\ U_{norm}(k_3, \omega) = \frac{abs(U_{r,fo})}{max(U_{r,\theta,z})} \end{cases} \quad (6)$$

198 where  $U_r$ ,  $U_\theta$ ,  $U_z$  are respectively the radial, angular and axial (along  $(e_3)$ )  
 199 displacement through all the layers.  $U_{r,fo}$  is the radial displacement at the  
 200 top surface of the outer fluid. In the case where no outer fluid is present in the  
 201 model,  $U_{r,fo}$  is replaced by  $U_{r,s}$ , the radial displacement at the top surface  
 202 of the solid layer. Fig. 2(a) illustrates an example of the excitability of  
 203 guided wave modes in a cylindrical model with the presence of the outer fluid  
 204 layer model as a function of frequency. The color of each circle indicates the  
 205 amplitude of the mode excitability for each corresponding mode. Meanwhile,  
 206 Fig. 2(b) presents the mode shapes associated with a selected mode shown in  
 207 Fig. 2(a), highlighting the various displacements utilized in the calculation  
 208 of excitability.

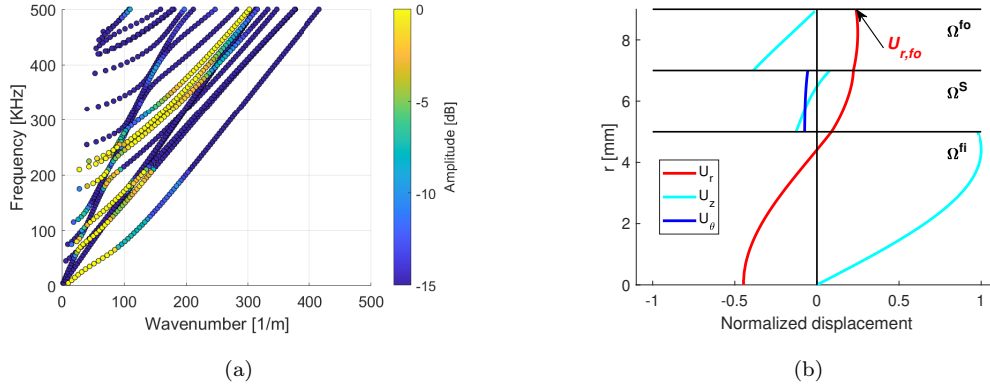


Figure 2: (a) Guided modes dispersion curves with their frequency-dependent excitability computed by SAIGA for a 3D cortical bone cylinder ( $\rho = 2310$  kg/m<sup>3</sup>,  $c_P = 2900$  m/s,  $c_S = 1600$  m/s,  $h^S = 2$  mm,  $r^S = 7$  mm) filled with soft tissue ( $\rho^{fi} = 1010$  kg/m<sup>3</sup>,  $c_P^{fi} = 1400$  m/s) and immersed in 2 mm of water. The color scale shows the excitability of each mode in dB normalized to the mode with the highest excitability at each frequency. (b) Mode shape of a selected mode ( $f = 200$  kHz and  $k = 127$  m<sup>-1</sup>).

## 209 2.2. Inversion algorithm

210 This study hypothesizes that aligning experimental dispersion curves with  
 211 the simulated ones generated via the SAIGA method can effectively evaluate  
 212 the properties of the cortical bone layer ( $c_P$ ,  $c_S$ ,  $h^S$  and  $r^S$ ). To do so, an  
 213 inversion algorithm was developed using a cost function as a metric to de-  
 214 termine the optimal alignment between the experimental dispersion curves  
 215 and specific instances within the simulated dataset. It is worth mentioning  
 216 that the accuracy of the method depends on several factors, including the  
 217 quality of experimental dispersion curves, the accuracy of the phantom ge-  
 218 ometry and mechanical properties in the model, and of parameters used for  
 219 numerical simulations such as the order of the NURBS basis function, grid  
 220 steps of the simulated dataset and the overall precision of the model.

221 *2.2.1. Formulation of the cost function*

222 By definition, a cost function is a metric to gauge the difference be-  
 223 tween predicted values from a model, and experimental observations. The  
 224 minimization of the cost function typically leads to the best fit between  
 225 the numerical and experimental data. However, the formulation of the cost  
 226 function may alter the output result and influence the algorithm’s perfor-  
 227 mance. Here, dispersive trajectories and excitability of ultrasonics guided  
 228 waves modes were used and we employed the same cost function as Chaboty  
 229 *et al.* used in [27]. The robustness of this function has been successfully  
 230 validated on a bi-layer plate model. Therefore, the cost function quantifies  
 231 the difference in magnitude between actual and simulated dispersive curves.

232 Considering a set of parameters  $\Lambda=(\rho, c_P, c_S, h^S, r^S)$  and  $\Lambda=(\rho, c_P,$   
 233  $c_S, h^S, r^S, h^{fo})$  in the case of the phantom in a free-field and of an im-  
 234 mersed phantom respectively, the difference of amplitude for each simulated  
 235 frequency was calculated as follows:

$$d_n(\Lambda, f) = |Ex(k_n(\Lambda), f) - A(k_n, f)|, \quad (7)$$

236 where  $Ex(k_n(\Lambda), f)$  represents the simulated excitability of a particular mode  
 237 at wavenumber  $k_n$  and frequency  $f$  for a given set of parameter  $\Lambda$ . Similarly,  
 238  $A(k_n, f)$  is the experimental amplitude observed for the couple  $(k_n, f)$ .

239 To prioritize higher-amplitude modes in the inversion process, a weighting  
 240 factor was introduced. This factor ensured that modes with amplitudes below  
 241 a user-defined threshold,  $\xi$ , were discarded from the cost function, while  
 242 those with the highest amplitudes contributed fully, with a weight of 1. The

243 weighting factor was defined as:

$$\chi_n(\Lambda, f) = \frac{Ex(k_n(\Lambda), f) - \xi}{-\xi} \quad (8)$$

244 Using these two indicators,  $d_n(\Lambda, f)$  and  $\chi_n(\Lambda, f)$ , the cost function for a  
245 particular set of parameters  $\Lambda$  was defined as:

$$J(\Lambda) = \sum_f \sqrt{\sum_{n=1}^N (d_n(\Lambda, f) \cdot \chi_n(\Lambda, f))^2} \quad (9)$$

246 where  $N$  is the total number of simulated modes for a given frequency. This  
247 cost function thus emphasizes high-amplitude modes while disregarding those  
248 below the threshold, reducing the risk of incorporating irrelevant information  
249 into the inversion. In this study the threshold  $\xi$  was fixed at -15 dB. In sum-  
250 mary, this cost function calculates the accumulation of errors between the  
251 model predictions (for a parameters set ( $\Lambda$ )) and the experimental observa-  
252 tions:  $d_n(\Lambda, f)$ , weighted by  $\chi_n(\Lambda, f)$ . The objective is to minimize the value  
253 of  $J(\Lambda)$  by adjusting the set of parameters ( $\Lambda$ ).

254 To ensure compliance with thermodynamic principles and to avoid ob-  
255 taining results lacking physical meaning or deviating significantly from val-  
256 ues reported in the literature [41, 42, 43, 27], the Poisson's ratio was calcu-  
257 lated for each parameter set  $\Lambda$ . Based on reference wave velocity values for  
258 the two bone phantoms (see Table 2), the experimental Poisson's ratios for  
259 the healthy and osteoporotic cylinders were 0.2365 and 0.2475, respectively.  
260 Consequently, a condition was imposed on the Poisson's ratio  $\nu(\lambda)$  for each  
261 parameter set. If  $0.22 < \nu(\lambda) < 0.26$ , the set was included in the inversion  
262 process; otherwise, it was excluded.

263 *2.2.2. Dataset generation*

264 The cost function was calculated for all sets of simulated properties. Each  
265 parameter was systematically swept across a multidimensional grid. The  
266 range of each parameter was chosen to be large enough to incorporate both  
267 properties of the healthy and osteoporotic bone phantom cylinder. Each  
268 parameter range was defined large enough to ensure that the measured bone  
269 phantom cylinder properties were far enough from the limit values.

270 Two sets of data were generated. One represented the scenario of free-  
271 field bone phantom cylinders, while the other depicted those immersed in  
272 olive oil. To reduce computation time, the decision was made to maintain  
273 the mechanical properties of both inner and outer fluids constant. The inner  
274 portion of the bone phantom cylinder is made of soft tissue-mimicking ma-  
275 terial. Both phantoms were manufactured by the same company that makes  
276 the plates in [27]. It was assumed that the properties of the soft tissue mim-  
277 icking material remain identical. Therefore,  $\rho^{fi} = 977 \text{ kg/m}^3$  and  $c_P^{fi} = 1390$   
278 m/s. Properties of the outer fluid correspond to those of olive oil and will  
279 remain constant:  $\rho^{fo} = 913 \text{ kg/m}^3$  and  $c_P^{fo} = 1455 \text{ m/s}$ . Table 1 depicts the  
280 parameters grid.

281 Parameter steps were chosen by balancing resolution and computational  
282 efficiency. Concerning the free-field model, a single simulation took approx-  
283 imately 45 seconds, whereas in the immersed model, it took nearly 70 sec-  
284 onds. The server used for calculations was a high-performance GPU-based  
285 system, 256GB of RAM, with dual Xeon Silver 4215 processors (16 cores,  
286 32 threads) which enabled parallelization of the calculus. For both datasets,  
287 the total number of cases was 3072 and 9216, respectively. Emphasizing the

	Parameters range	Step
$\rho$ (kg/m <sup>3</sup> )	[1900 - 2500]	200
$c_P$ (m/s)	[2450 - 3150]	100
$c_S$ (m/s)	[1400 - 1900]	100
$r^S$ (mm)	[9 - 10.5]	0.5
$h^S$ (mm)	[2.7 - 3.3]	0.2
$h^{fo}$ (mm)	[2.5 - 3.5]	0.5

Table 1: Range of model parameters and their respective step used to create the datasets.

288 importance of including all modes, a frequency resolution step size of 5 kHz  
289 was chosen, allowing for 90 frequencies to be measured within the 50-500 kHz  
290 frequency range. Two comprehensive databases regrouping all the possible  
291 cases of both scenarios were created during an extended, continuous mod-  
292 eling session. The free-field database required 36 hours to complete, while  
293 the immersed database took 180 hours (7.5 days) for simulations. Generat-  
294 ing datasets for 2.5D models requires a much higher cost compared to 1.5D  
295 problems. In our previous study [27], generating 72,600 cases for a 1.5D bi-  
296 layer plate model took less than 48 hours for computation without using the  
297 parallelization.

### 298 *2.3. Experimental protocols*

#### 299 *2.3.1. Bone phantom cylinders and reference values*

300 In this study, two bone phantom cylinders filled with soft tissue-mimicking  
301 material were used: one with properties considered as healthy, and the other  
302 simulating an osteoporotic state with degraded properties. These cylindrical

303 specimens were made by True Phantom Solutions (Windsor, ON, Canada),  
304 are 150 mm long and have a diameter of 20 mm, with a cortical layer thick-  
305 ness of around 3 mm. Additionally, two small blocks representing healthy  
306 and osteoporotic cortical layers were provided. Pulse-echo measurements  
307 were conducted on these blocks to establish baseline sound velocity values.  
308 The sample thicknesses were measured 20 times, followed by an equivalent  
309 number of pulse-echo measurements. For these pulse-echo measurements, a  
310 longitudinal probe (V125-RM) and a shear probe (V124-RM) from Olympus  
311 centred at 2.25 MHz were employed. An Omniscan-X3 from the same com-  
312 pany was used to perform the measures. Densities were also calculated based  
313 on these samples by weighting them and measuring their volume with a 3D  
314 laser scanner (Absolute Arm 85) from Hexagon (Stockholm, Sweden), with  
315 uncertainties for each parameter derived from the measurements. To pre-  
316 cisely determine the thickness of the cortical phantom layer of each cylinder,  
317 36 measurements were taken across all the phantoms using the longitudinal  
318 probe. The baseline velocity values obtained with the block specimens were  
319 used to determine the actual thickness of the cortical layer of the cylinders.  
320 It was assumed that the cortical layer has nearly-isotropic behavior and was  
321 homogeneous. However, the cross-section's geometry of the phantoms were  
322 not uniform along their length. In fact, a variation of around 10% was ob-  
323 served in the cortical thickness and diameters. As a result, the mean values  
324 will be used for comparison with the inversion results.

### 325 *2.3.2. Axial transmission setup*

326 A probe was specifically designed and built to perform the ultrasonic ex-  
327 citation. The components have been chosen to provide a central frequency of

328 350 kHz with -6 dB bandwidth between 150 kHz and 550 kHz. The selected  
329 frequency range enables the extraction of the bone mechanical properties as  
330 well as the geometry, making it suitable for a 4 mm thick cylinder. This  
331 range can be adjusted based on the target site. Low frequencies are inter-  
332 esting for capturing the full cross-section and retrieving both thickness and  
333 radius, while the upper frequency limit can be adapted to obtain the de-  
334 sired number of modes for the inverse process to converge. A combination of  
335 specific piezoelectric and matching layer components was used to maximize  
336 the transmission of the waves through the bone phantom. Hann windowed  
337 tonebursts with a maximum amplitude of 12V were used to excite the piezo-  
338 electric element, with central frequencies varying from 50 kHz to 500 kHz  
339 with a step of 50 kHz. The number of cycles was chosen specifically to en-  
340 sure each toneburst has a bandwidth at -3 dB of  $\pm 50$  kHz. The probe has  
341 a dimension of 20x4 mm with a flat front surface.

342 For the free-field measurements, where cylinders are not immersed in fluid,  
343 the probe was placed in contact with the outer perimeter of the cylinders and  
344 coupled with an ultrasonic gel Ultragel® II. A guide ensures the probe is  
345 placed normal to the surface with the 20 mm dimension perpendicular to  
346 the axis of the cylinders. For the immersed case, a constant outer fluid layer  
347 of approximately 3 mm was maintained, with the sensor positioned slightly  
348 below the top surface of the fluid. For this, a 3 mm-thick spacer was placed  
349 between the cylinder's surface and the probe's face. Positioning is done using  
350 the same guide as for the case in air. Once the probe is in place, it is held by a  
351 clamp, and the spacer is carefully removed. The probe is therefore positioned  
352 3 mm above the cylinder's surface, perpendicular to the fluid's surface.

353 Four consecutive acquisitions were realized on the cylinders for both sce-  
354 narios. After each acquisition, the probe was repositioned and slightly shifted  
355 aside for averaging the impact of its position. Acquisitions were carried out  
356 along the bone phantom axis at 60 equally spaced positions, 1 mm apart,  
357 using a Doppler laser vibrometer (Polytech OFV-505). Two of the four ac-  
358 quisitions were conducted in one direction, with the remaining two measure-  
359 ments performed in the opposite direction, to minimize the effect of possible  
360 thickness variations within the fluid layer. In the immersed configuration,  
361 the laser was focused on the fluid's surface. The reflective properties of olive  
362 oil, attributed to its green hue, facilitated effective signal detection. Con-  
363 ducting the experiments in a darkened environment further enhanced the  
364 signal quality.

365 A TiePie® Handyscope HS3 was used to send the emitting signals to  
366 the probe and to acquire the data measured by the laser vibrometer. Ex-  
367 perimental data were processed with a 2D fast Fourier transform to obtain  
368 experimental dispersion curves [44]. Fig. 3 represents a photograph of the  
369 experimental setup along with representative time trace signals recorded in  
370 the immersed configuration. These signals represent ultrasonic guided waves  
371 measured on the healthy bone phantom immersed in olive oil at points 1,  
372 30, and 60. The waveform evolution during propagation is clearly observed.  
373 Despite being the least favorable case, a satisfactory SNR of 30 dB was ob-  
374 tained.

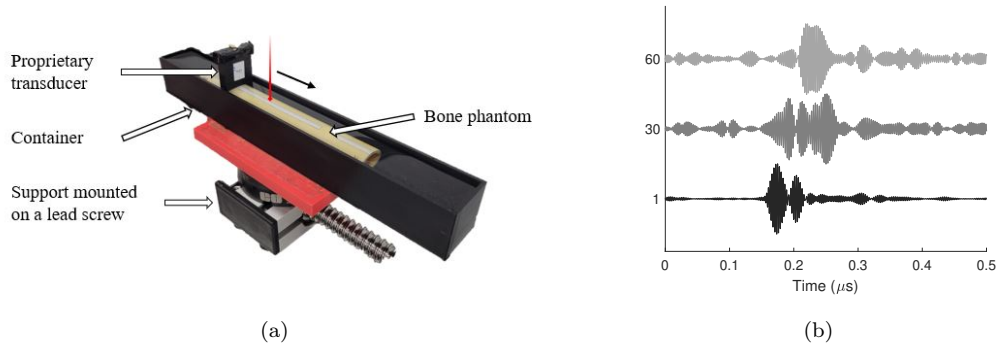


Figure 3: (a) Experimental setup used for the axial transmission measurements with bone phantom cylinder immersed in fluid. (b) Representative signals for the immersed case at measurement points 1, 30 and 60.

### 375 **3. Results**

#### 376 *3.1. Bone phantom cylinder properties*

377 Pulse-echo measurements were conducted to establish the reference values  
 378 that will be used in the inversion process. As explained in section 2.3.1, the  
 379 geometric cross-section of the cortical layer of both cylinders is not uniform  
 380 along their length, with a variation of about 10%. Nonetheless, the cortical  
 381 synthetic material is assumed to be isotropic and homogeneous throughout  
 382 the phantoms. Reference values of the cortical layer for both the healthy  
 383 phantom and the osteoporotic one are depicted in Table 2.

#### 384 *3.2. Parameters sensitivity*

385 A study was conducted to evaluate how different parameters affect the  
 386 dispersive trajectories of the ultrasonic guided wave modes. To this end, a  
 387 variation of  $\pm 10\%$  was applied to each parameter to assess its influence. The

	Healthy bone phantom	Osteoporotic bone phantom
$\rho$ (kg/m <sup>3</sup> )	2295 $\pm$ 35	2085 $\pm$ 20
$c_P$ (m/s)	2945 $\pm$ 65	2650 $\pm$ 35
$c_S$ (m/s)	1730 $\pm$ 25	1535 $\pm$ 15
$r^S$ (mm)	9.77 $\pm$ 0.50	9.96 $\pm$ 0.53
$h^S$ (mm)	3.00 $\pm$ 0.23	2.97 $\pm$ 0.29

Table 2: Reference property values for the healthy and osteoporotic bone phantom cylinders.

reference chosen parameters correspond to the central value of each parameter's range presented in Table 1. The variations were applied to  $c_P$  while keeping  $\nu$  constant and equal to 0.24 (thus causing  $c_S$  to vary accordingly), as well as to  $r_S$ ,  $h^S$ , and  $h^{fo}$ . The results are presented in Fig. 4. To observe the effect of each parameter on the dispersion curve trajectories, only mode points with an excitability value greater than  $-3$  dB are retained.

Fig. 4 shows that variations of  $c_P$ ,  $c_S$  and  $r_S$  globally influence the trajectories of dispersion curves, while  $h^S$  primarily affects low frequencies and  $h^{fo}$  impacts higher frequencies emphasizing the importance of using low frequency to minimize the impact of soft tissue layer. However, the variations presented in Fig. 4 are the result of modifying only one parameter at a time. Osteoporosis likely induce a simultaneous decrease of cortical thickness and wave velocities [24], further amplifying the differences between healthy and osteoporotic bone. This emphasizes the necessity of assessing all bone parameters simultaneously rather than each one independently.

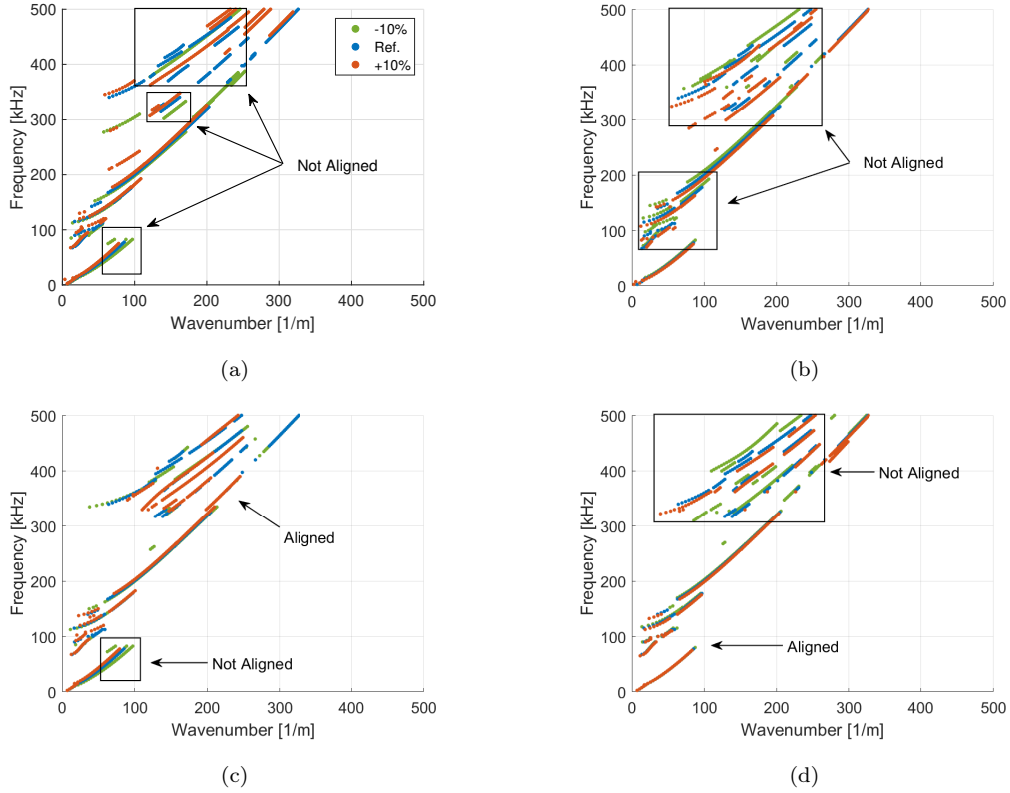


Figure 4: Effect of parameter variations on ultrasonic guided waves dispersion curves. The blue lines represent the reference curves, the green lines correspond to the  $-10\%$  variation, and the orange line to the  $+10\%$  variation. Parameter influences are shown for: (a)  $c_P$  with  $\nu$  held constant, (b)  $r^S$ , (c)  $h^S$ , and (d)  $h^{f^o}$ . Arrows and rectangles highlight the key areas where changes take place.

### 403 3.3. Dispersion curves fitting

404 Experimental acquisitions were carried out with both phantoms under two  
 405 conditions: with and without the outer fluid. Four measurements were taken  
 406 for each case along the axis of the bone cylinders to extract experimental  
 407 dispersion curves. The inversion procedure was then applied to both the  
 408 healthy and osteoporotic phantoms in each scenario.

409 *3.3.1. Dispersion curve fitting for free-field bone phantom cylinders*

410 The experimental results shown in Fig. 5 are obtained by averaging the  
411 2D-FFT plots for the corresponding four separate axial transmission mea-  
412 surements obtained for each cylinder. Averaging allows to consolidate spatial  
413 frequency information across multiple measurements to enhance clarity of the  
414 visual analysis. The semi-analytical points predictions are superimposed on  
415 the experimental dispersion curves with a -3 dB threshold applied to improve  
416 clarity. All values below -3 dB are automatically discarded to enhance visibil-  
417 ity. As shown in Fig. 5, the alignment between experimental and simulated  
418 dispersion curves shows a good agreement for both phantoms, especially con-  
419 cerning the tangential slope of the curves, despite some differences that will  
420 be discussed in the next section.

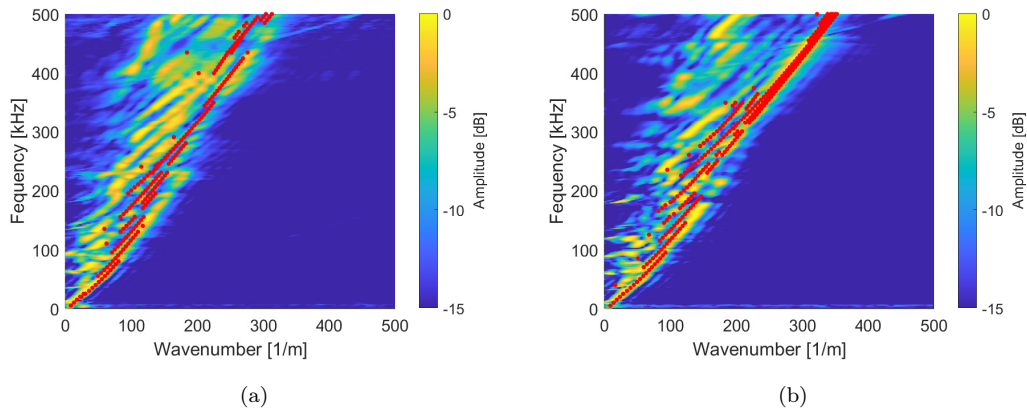


Figure 5: Optimal fit between experimental and simulated dispersion curves for (a) healthy phantom, and (b) osteoporotic phantom. SAIGA-computed best fit are depicted by the red points atop experimental curves.

421 *3.3.2. Dispersion curve fitting for immersed bone phantom cylinders*

422 In order to be closer to *in-vivo* conditions, the cylinders were immersed  
423 in a viscous fluid. The rationale is that the immersed setup provides a more  
424 accurate representation of real-world conditions. Olive oil was found to be a  
425 good candidate for this. In line with Mast’s empirical study [34] and other  
426 relevant research [45], the suggested range for soft tissue density is between  
427  $900 \text{ kg/m}^3$  and  $1200 \text{ kg/m}^3$ . As mentioned in Section 2.2.1, olive oil was  
428 chosen thanks to its higher attenuation relative to water, while having sim-  
429 ilar sound speed and density to soft tissue. A layer of fluid was established  
430 atop the bone phantom cylinders, measuring 3 mm in thickness. The probe  
431 was positioned slightly below the fluid’s surface, ensuring partial immersion.  
432 Results are presented similarly to Section 3.3.1. The semi-analytical point  
433 predictions are superimposed on the experimental dispersion curves with a  
434 -3 dB threshold. Fig. 6 corresponds to the best-fitting scenario for both  
435 cylinders. Due to the presence of olive oil surrounding the bone phantom  
436 cylinder, measurements were noisier in comparison with the free field sce-  
437 nario. Therefore, horizontal perturbations can be seen on the experimental  
438 dispersion curves for the immersed case.

439 *3.4. Estimation of bone phantoms’ properties*

440 The average inverse characteristics for the four axial transmission mea-  
441 surements, optimized for each cylinder, are presented in Tables 3 and 4  
442 for the free-field and immersed scenario, respectively, along with reference  
443 properties and their relative errors. Results demonstrate a close alignment  
444 of the mechanical property values, with errors below 3.0% for both scenarios.  
445 However, a larger discrepancy was obtained for the thickness and radius of

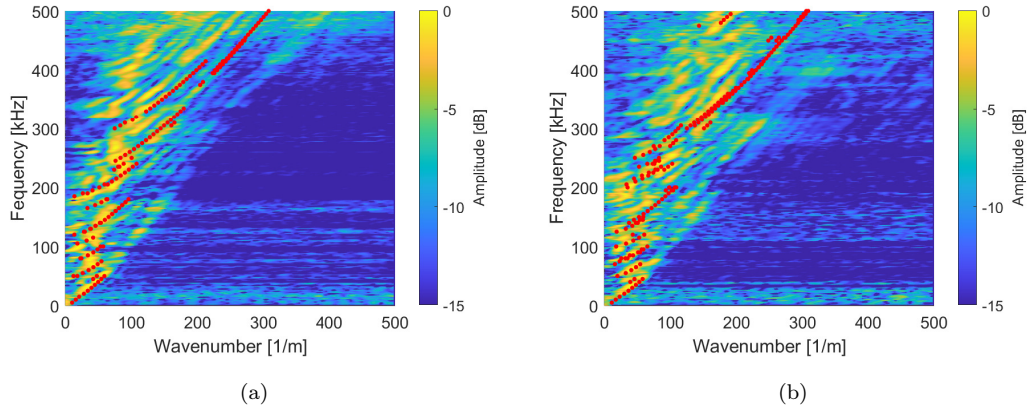


Figure 6: Optimal fitting results between experimental and simulated dispersion curves for (a) healthy phantom cylinder, and (b) osteoporotic phantom cylinder immersed in olive oil. SAIGA-computed best fit are depicted by the red points atop experimental curves.

446 the cortical shell for the free field case, which may be due to the fact that  
 447 these parameters are inconsistent along the bone phantoms, and that their  
 448 variations were averaged out during pulse-echo measurements.

449 In the free-field case, as shown in Fig. 5, the simulated dispersion curves  
 450 align closely with the high-wavenumber modes across all frequencies. Conse-  
 451 quently, the slope of the experimental curves is accurately captured, leading  
 452 to precise predictions of the inverted properties such as wave velocities.

453 In contrast, for the immersed case in Fig. 6, the simulated dispersion  
 454 curves align better at low frequencies with the low-wavenumber modes. This  
 455 results in more accurate estimations of the geometrical parameters, empha-  
 456 sizing the critical role of low-frequency modes in determining bone geometry.

	Healthy Cylinder			Osteo. Cylinder		
	Ref.	Inv.	Err.%	Ref.	Inv.	Err.%
$c_P$ (m/s)	$2945 \pm 65$	$2950 \pm 141$	0.17	$2650 \pm 35$	$2650 \pm 115$	0.00
$c_S$ (m/s)	$1730 \pm 25$	$1725 \pm 95$	0.29	$1535 \pm 15$	$1550 \pm 58$	0.98
$r^S$ (mm)	$9.77 \pm 0.50$	$10.13 \pm 0.75$	3.63	$9.96 \pm 0.53$	$9.25 \pm 0.29$	7.13
$h^S$ (mm)	$3.00 \pm 0.23$	$2.90 \pm 0.23$	3.63	$2.97 \pm 0.29$	$3.3 \pm 0.0$	11.11

Table 3: Average inverse properties of phantom cylinders with their relative errors for the free-field scenario.

	Healthy Cylinder			Osteo. Cylinder		
	Ref.	Inv.	Err.%	Ref.	Inv.	Err.%
$c_P$ (m/s)	$2945 \pm 65$	$3025 \pm 95$	2.72	$2650 \pm 35$	$2700 \pm 100$	1.89
$c_S$ (m/s)	$1730 \pm 25$	$1750 \pm 58$	1.16	$1535 \pm 15$	$1575 \pm 50$	2.61
$r^S$ (mm)	$9.77 \pm 0.50$	$9.75 \pm 0.65$	0.20	$9.96 \pm 0.53$	$9.75 \pm 0.65$	2.11
$h^S$ (mm)	$3.00 \pm 0.23$	$2.90 \pm 0.28$	3.33	$2.97 \pm 0.29$	$3.1 \pm 0.28$	4.38

Table 4: Average inverse properties of phantom cylinders with their relative errors for the fluid-immersed scenario.

#### 457 3.4.1. Estimated bulk-wave velocities

458 According to Tables 3 and 4, the average predicted values for longitudinal  
459 and shear wave velocities remain within the tolerance range of the reference  
460 values for both cylinders in all situations. In the free-field scenario, the error  
461 is found to be lower than 1%, while it slightly increases in the immersed  
462 scenario, albeit still remaining below 3%. This increase can be attributed  
463 to fluctuations in the surrounding fluid's thickness as well as its material

464 properties due to changes in the experimental environment (change in oil  
465 temperature for example). Moreover, due to the presence of the outside  
466 fluid, experimental data are found to be much noisier, resulting in slight  
467 variation during the inversion.

#### 468 3.4.2. *Estimated radius and thickness*

469 The estimated values of the thickness  $h^S$  and radius  $r^S$  fall within the  
470 baseline measurement margins of error. However, the relative errors are  
471 larger in the free-field case. The curvature of the bone phantom cylinders  
472 creates nearly point-like contact between the probe and the cortical shell,  
473 resulting in the generation of numerous circumferential modes. This com-  
474 plexity increases the challenge of fitting the dispersion curves accurately. In  
475 this specific case, the dispersion curves aligned more effectively with high-  
476 wavenumber modes, leading to more accurate velocity predictions but less  
477 precision in estimating the geometry. In contrast, when the cylinders are  
478 immersed in the fluid, this phenomenon is decreased as wave generation oc-  
479 curs over a broader area. Also, the dispersion curves aligned more effectively  
480 with low-wavenumber modes, which are strongly representative of the bone  
481 geometry.

482 Moreover, the osteoporotic cylinder has greater errors in radius and thick-  
483 ness measurements in both scenarios. This discrepancy may come from the  
484 overall geometry of the bone phantom as explained in Section 2.1.1. Ad-  
485 ditionally, reference values for cortical thickness in the osteoporotic model  
486 carry greater uncertainties. These subtle differences cumulatively result in  
487 larger percentage deviations during the inverse transformation.

488 *3.4.3. Error propagation through the inversion process*

489 The inversion process involves two main sources of uncertainty: grid dis-  
490 cretization and experimental variability.

491 The grid resolution sets the precision of the parameter estimates. A finer  
492 grid improves accuracy but increases computational cost, while a larger grid  
493 step can introduce systematic errors. In this study, the parameter step sizes  
494 were chosen to balance these factors (see Section 2.2.2). For example, the  
495 step size for  $c_P$  is 100 m/s, leading to an uncertainty of  $\pm 50$  m/s due to grid  
496 discretization which remain in the uncertainties range of the reference values,  
497 the same can be observed for other parameters. The relative errors for  $c_P$   
498 and  $c_S$  (below 3%) confirm that the chosen resolution is appropriate.

499 We performed also four independent measurements on each cylinder.  
500 Each of the four axial transmission measurements was subject to experi-  
501 mental uncertainties, including noise, boundary inconsistencies, and slight  
502 variations in the bone phantom geometry. These uncertainties propagated  
503 through the cost function and affected the estimated parameters.

504 The reported standard deviations in Tables 3 and 4 for the inverted prop-  
505 erties reflect the combined effects of these experimental uncertainties and grid  
506 resolution. For instance, the larger discrepancies observed for the radius ( $r^S$ )  
507 and cortical thickness ( $h^S$ ) can be attributed to physical variations in the  
508 bone phantoms that are averaged out during the pulse-echo measurements.  
509 This averaging reduces the sensitivity of the inversion to localized inconsis-  
510 tencies but increases the relative error for these parameters compared to  $c_P$   
511 and  $c_S$ .

512 *3.4.4. Assessment of cortical layer density*

513 Density is not directly assessed through the inversion process, but rather  
514 with a mathematical model [15, 40]. As the model used in the simulation  
515 is isotropic, the resulting model parameters, which reflect the waveguide’s  
516 stiffness, consist of two bulk wave velocities  $c_P$  and  $c_S$ , incorporating the  
517 mass density within the velocity parameters [16, 46, 47, 48] and a stiffness  
518 ratio of elastic coefficients  $C_{11}/C_{13} = 1 - 2(c_S/c_P)^2$ . Using the reference  
519 values for density and bulk wave velocities, a linear interpolation can be  
520 made to express  $C_{11} = \rho c_P^2$  and  $C_{66} = \rho c_S^2$  as a function of density  $\rho$  [27]. As  
521 a consequence,  $c_P$  and  $c_S$  can also be expressed as a function of density as  
522 shown in Fig. 7.

523 Using inverse properties of both scenarios, density can be determined for  
524 the healthy and osteoporotic cylinder. As a result, for the free-field case, the  
525 results yield  $\rho = 2300 \pm 10 \text{ kg/m}^3$  and  $\rho = 2096 \pm 12 \text{ kg/m}^3$  for the healthy  
526 and osteoporotic cylinder respectively, leading to relative errors of 0.17%  
527 and 0.53%. For the immersed case, the density of healthy and osteoporotic  
528 cylinders are found to be respectively  $\rho = 2343 \pm 28 \text{ kg/m}^3$  and  $\rho = 2120 \pm 5$   
529  $\text{kg/m}^3$ , with relative errors of 2.09% and 1.68%, which are quite acceptable  
530 at this stage.

531 **4. Discussion**

532 The cost function was computed across a multi-dimensional model grid,  
533 consistently identifying a global minimum for each acquisition. While navi-  
534 gating five or six dimensions is computationally demanding, SAIGA processes  
535 an immersed case in just over a minute but requires about eight days for all

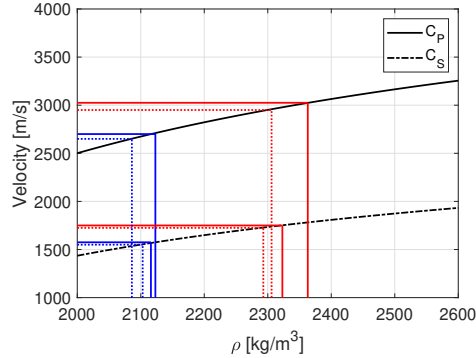


Figure 7: Bulk velocities varying with the bulk density of the phantoms cortical material. (Blue lines) Inverse values for longitudinal and shear velocities of Osteoporotic phantom cylinder. (Red lines) Inverse values for longitudinal and shear velocities of Healthy phantom cylinder. Full lines depict the inverse values retrieved in the immersed scenario and the dot lines correspond to the free-field case scenario without outside fluid.

536 9216 scenarios. However, since the dataset is generated once, subsequent  
 537 inversions take only minutes. Using a parameter sweep over a finite set en-  
 538 sures a consistent global minimum, eliminating optimization concerns. Yet,  
 539 predefined grid steps may introduce bias, though they were chosen to align  
 540 with reference value uncertainties.

541 As mentioned in the previous study from our group [27], incorporating  
 542 modal excitability into the cost function was crucial to improve the inversion  
 543 procedure, significantly reducing the number of relevant modes. This re-  
 544 duction was achieved by weighting modes according to their excitability. By  
 545 including only a limited number of modes, this approach minimizes data mis-  
 546 fits during inversion. As demonstrated by Chaboty *et al.* [27], incorporating  
 547 excitability into the inversion process reduces the percentage error by more  
 548 than 10% compared to an inversion without this parameter. This methodol-

549 ogy has proven effective in a 2.5D case scenario. Excitability ensures that all  
550 modes exhibiting high amplitudes are taken into account. Without incorpo-  
551 rating excitability, the inversion process may be biased toward modes with  
552 high amplitudes over a broad frequency spectrum while neglecting lower-  
553 amplitude modes or those with high amplitudes over a narrow frequency  
554 range, which are particularly representative of geometry at low frequencies.  
555 This aspect is crucial as it allows for the inversion of the entire bone geome-  
556 try rather than being limited to thickness estimation, as commonly observed  
557 in the literature where higher frequencies are employed. Furthermore, the  
558 relative errors obtained in our study remain within the same range as those  
559 reported by Bochud *et al.* and Minonzio *et al.*, consistently below 5% [47, 48].

560 Despite a favorable correlation between experimental and simulated re-  
561 sults, especially at low frequencies ( $< 200$  kHz) where curves aligned with  
562 great accuracy, there are discrepancies in the alignment of experimental and  
563 SAIGA-reconstructed dispersion curves at higher frequencies, as shown in  
564 Figs. 5 and 6. Several factors contribute to these differences.

565 Firstly, the accuracy of the SAIGA simulation-based approach hinges on  
566 the precision of the underlying model. Seyfaddini *et al.* [29] have demon-  
567 strated, through a comparison between SAIGA and the DISPERSE analyt-  
568 ical model [49], that the number of degrees of freedom  $N_{dof}$  in the model  
569 is crucial for obtaining accurate results. While SAIGA remains significantly  
570 more efficient than the SAFE method, it still requires a sufficiently large  
571 value of  $N_{dof}$  to maintain precision. Unfortunately, increasing the accuracy  
572 and so the value of  $N_{dof}$  exponentially increases computation time. In the  
573 case presented in this manuscript, since the region of interest includes low

574 frequencies, the number of patches of the model and the order of NURBS  
575 basis functions are considered acceptable, knowing that a single case takes  
576 around 70 seconds to compute. Doubling the number of elements would re-  
577 sult in a simulation time of approximately 15 minutes. As a consequence, it  
578 would take around 96 days to process the 9216 cases required for this study,  
579 given our current computational capabilities. However, the inversion of the  
580 cortical bone phantom has yielded promising outcomes using the selected pa-  
581 rameters, potentially indicating improved forecasts if the model's precision  
582 is enhanced.

583 Secondly, the complex geometry of cortical bone has been approximated  
584 by a cylindrical-like structure, making strong assumptions of symmetrical  
585 conditions. However, as shown in Fig. 1(b,c), the actual bone shape is not  
586 perfectly symmetric. Therefore, a difference in the simulated shape model  
587 and the real experimental geometry can explain such differences at higher  
588 frequencies. Nonetheless, estimated thickness and properties are found to be  
589 close to the reference ones, as shown in Table 3 and 4.

590 The quality of experimental measurements is critical to the inversion pro-  
591 cess. The curvature of bone phantoms necessitates precise probe alignment  
592 with laser spots to extract dispersion curves accurately, as misalignment re-  
593 duces amplitude and introduces variability. To mitigate this, multiple ac-  
594 quisitions were performed, though some variations persist. The cylindrical  
595 shape also supports circumferential modes, complicating inversion. However,  
596 since the method targets the radius, its asymmetry suppresses these modes,  
597 simplifying guided wave visualization. This suggests that the inversion pro-  
598 cess may be less sensitive to measurement fluctuations, particularly in *in-vivo*

599 applications.

600 Finally, the properties of the cortical layer were defined as isotropic to  
601 match the phantoms used in this study. However, it is well known that  
602 cortical bones exhibit anisotropic or, at the very least, orthotropic behavior.  
603 To adapt the proposed method for *in vivo* bone characterization, the model  
604 should be further developed to account for the complexity of the medium.  
605 Future iterations could adopt approaches similar to those proposed by Pereira  
606 *et al.* [15, 50], where the elastic coefficients vary with density based on  
607 a homogenization scheme developed by Vu *et al.* [40]. Alternatively, the  
608 model could include multiple layers within the cortical thickness to represent  
609 bone degradation from the endosteal to the periosteal region [51, 11, 20, 17].

## 610 5. Conclusion

611 Using low frequencies in the context of axial transmission of ultrasonic  
612 guided waves demonstrated its ability to deduce the properties of bone cortex  
613 in an *in-vivo*-like configuration. The implementation of excitability requires  
614 fewer modes than other inversion techniques used at high frequencies. Us-  
615 ing a combination of multiple high-excitability mode segments, the proposed  
616 SAIGA model achieved successful alignment with the amplitude of experi-  
617 mental dispersion curves. The study presented here builds on the work of  
618 Chaboty et al. [27], and offers a promising proof of concept for using the  
619 method in a clinical assessment of cortical bone properties. However, several  
620 limitations must be considered. The assumption of a simplified cylindri-  
621 cal bone model, while computationally efficient, does not fully capture the  
622 anatomical variability of real bones, particularly the radius. The current

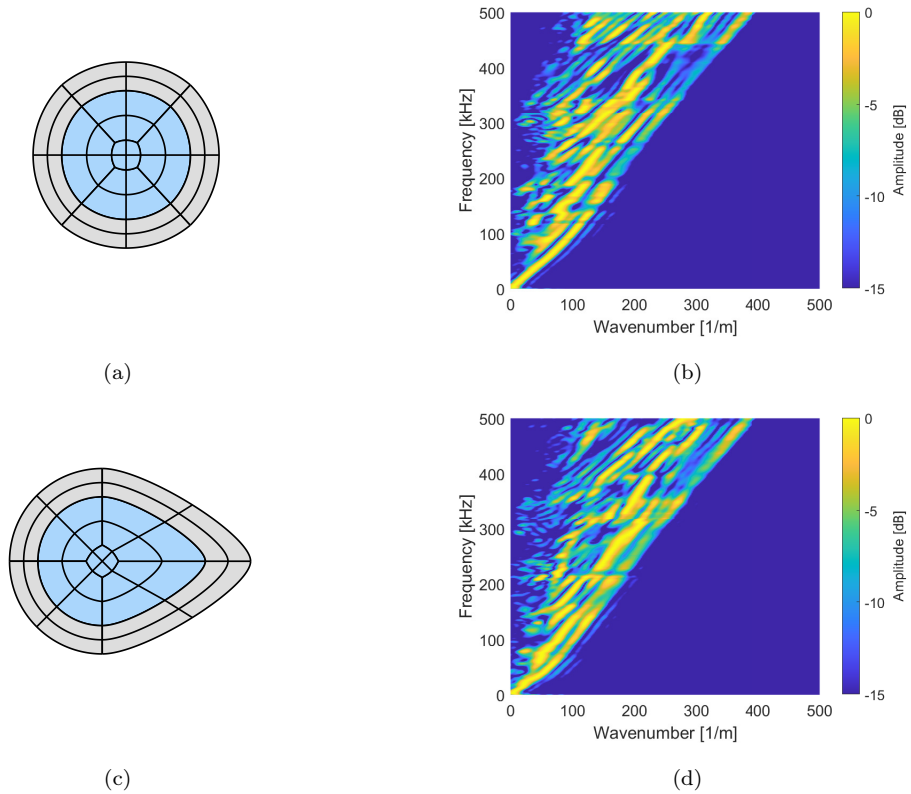


Figure 8: Differences between a cylindrical geometry and a radius-like geometry. (a,c) Geometry of the two models. (b,d) Corresponding dispersion curves showing that fewer modes exist in the radius model.

623 inversion scheme, although effective, remains computationally demanding,  
 624 limiting the size of the dataset. Additionally, the experimental setup re-  
 625 lies on precise alignment of the probe with laser measurements, which may  
 626 introduce errors in practical *in vivo* conditions. A multi-element axial trans-  
 627 mission probe must be developed to replace the use of laser measurements,  
 628 as this technique is too sensitive for human body measurements.

629 The model will later evolve into a radius-shape bone, as presented in the

630 discussion section. Improvements must be made to the SAIGA algorithm to  
631 reduce its computation time in order to increase the dataset with a smaller  
632 step for each parameter. The model will shift from an isotropic material to  
633 a transversely isotropic medium to better represent the bone cortex. Fur-  
634 thermore, the inversion scheme could be further improved using artificial in-  
635 telligence (AI) techniques. This would increase its robustness, allowing it to  
636 evaluate bone properties based on the dispersion trajectories and amplitudes  
637 of guided wave modes within the waveguide.

638 The proposed method shows potential for clinical applications by provid-  
639 ing a non-invasive tool to assess bone quality and detect early-stage osteo-  
640 porosis. However, challenges such as patient variability and device repro-  
641 ducibility must be addressed. Differences in bone geometry, such as cortical  
642 thickness and outer diameter, require robust algorithms to ensure consistent  
643 results across diverse populations. Additionally, variability in device perfor-  
644 mance necessitates standardized protocols and self-calibrating mechanisms.  
645 Large-scale validation studies and the development of a comprehensive refer-  
646 ence database would enhance the method's sensitivity and reliability. Collab-  
647 orations with clinicians will be key to integrating this approach into clinical  
648 workflows, ensuring it aligns with practical diagnostic needs.

#### 649 **CRediT authorship contribution statement**

650 **A.C:** Conceptualization, Methodology, Software, Validation, Formal anal-  
651 ysis, Investigation, Writing - Original Draft, Writing - Review & Editing.

652 **V-H.N:** Conceptualization, Methodology, Software, Writing - Review &  
653 Editing, Supervision. **G.H:** Conceptualization, Resources, Writing - Review

654 & Editing, Supervision. **P.B:** Conceptualization, Methodology, Resources,  
655 Writing - Review & Editing, Supervision, Funding acquisition.

## 656 **Acknowledgments and funding**

657 The authors would like to thank Nvidia for providing us with an Nvidia  
658 Quadro P6000 graphics card for our GPU simulations. This research was  
659 funded by Natural Sciences and Engineering Research Council of Canada:  
660 NSERC – RGPIN – 2020 – 05802. The authors acknowledge the support of  
661 the Laboratoire Franco-Canadien de Recherches Ultrasonores (LAFCUS).

## 662 **Authors declarations**

### 663 *Conflict of interest*

664 The authors have no conflicts to disclose.

### 665 *Declaration of generative AI and AI-assisted technologies in the writing pro-* 666 *cess*

667 During the preparation of this work the authors used ChatGPT in order  
668 to improve English writing. This AI tool was not used for scientific analysis or  
669 data interpretation. After using this tool, the authors reviewed and edited the  
670 content as needed and take full responsibility for the content of the published  
671 article.

## 672 **Data availability**

673 The data that support the findings of this study are available from the  
674 corresponding author upon reasonable request.

675 **References**

- 676 [1] World Health Organization, *Assessment of fracture risk and its appli-*  
677 *cation to screening for postmenopausal osteoporosis : report of a WHO*  
678 *study group*. World Health Organization, 1994.
- 679 [2] World Health Organization, *Guidelines for preclinical evaluation and*  
680 *clinical trials in osteoporosis*. World Health Organization, 1998.
- 681 [3] P. Laugier and G. Häiat, eds., *Bone Quantitative Ultrasound*. Dordrecht:  
682 Springer Netherlands, 2011.
- 683 [4] Agence de la santé publique du Canada, “L’ostéoporose,” Aug. 2014.  
684 Last Modified: 2024-02-15.
- 685 [5] P. Laugier and Q. Grimal, eds., *Bone Quantitative Ultrasound: New*  
686 *Horizons*, vol. 1364 of *Advances in Experimental Medicine and Biology*.  
687 Cham: Springer International Publishing, 2022.
- 688 [6] Q. Grimal, J. Grondin, S. Guérard, R. Barkmann, K. Engelke, C.-C.  
689 Glüer, and P. Laugier, “Quantitative ultrasound of cortical bone in the  
690 femoral neck predicts femur strength: results of a pilot study,” *Journal*  
691 *of Bone and Mineral Research: The Official Journal of the American*  
692 *Society for Bone and Mineral Research*, vol. 28, pp. 302–312, Feb. 2013.
- 693 [7] C.-C. Glüer, “Quantitative Ultrasound Techniques for the Assessment of  
694 Osteoporosis: Expert Agreement on Current Status,” *Journal of Bone*  
695 *and Mineral Research*, vol. 12, no. 8, pp. 1280–1288, 1997.

- 696 [8] D. Pereira, A. Le Duff, G. Painchaud-April, and P. Belanger,  
697 “Simulation-Based Inversion for the Characterization of Adhesively  
698 Bonded Joints Using Ultrasonic Guided Waves,” *IEEE Transactions on*  
699 *Ultrasonics, Ferroelectrics, and Frequency Control*, vol. 69, pp. 2400–  
700 2407, July 2022.
- 701 [9] L. Bai, K. Xu, D. Li, D. Ta, L. H. Le, and W. Wang, “Fatigue evalu-  
702 ation of long cortical bone using ultrasonic guided waves,” *Journal of*  
703 *Biomechanics*, vol. 77, pp. 83–90, Aug. 2018.
- 704 [10] A. Guha, M. Aynardi, P. Shokouhi, and C. J. Lissenden, “Identification  
705 of long-range ultrasonic guided wave characteristics in cortical bone by  
706 modelling,” *Ultrasonics*, vol. 114, p. 106407, July 2021.
- 707 [11] G. Haiat, S. Naili, Q. Grimal, M. Talmant, C. Desceliers, and C. Soize,  
708 “Influence of a gradient of material properties on ultrasonic wave propa-  
709 gation in cortical bone: Application to axial transmission,” *The Journal*  
710 *of the Acoustical Society of America*, vol. 125, pp. 4043–4052, June 2009.
- 711 [12] M. Sasso, G. Haiat, M. Talmant, P. Laugier, and S. Naili, “Singular value  
712 decomposition-based wave extraction in axial transmission: application  
713 to cortical bone ultrasonic characterization,” *IEEE Transactions on Ul-*  
714 *trasonics, Ferroelectrics and Frequency Control*, vol. 55, pp. 1328–1332,  
715 June 2008.
- 716 [13] K. M. Knapp, K. M. Knapp, G. M. Blake, T. D. Spector, and  
717 I. Fogelman, “Multisite Quantitative Ultrasound: Precision, Age- and  
718 Menopause-Related Changes, Fracture Discrimination, and T-score

- 719       Equivalence with Dual-Energy X-ray Absorptiometry,” *Osteoporosis In-*  
720       *ternational*, vol. 12, pp. 456–464, June 2001.
- 721 [14] D. Hans, L. Genton, S. Allaoua, C. Pichard, and D. O. Slosman,  
722       “Hip Fracture Discrimination Study,” *Journal of Clinical Densitometry*,  
723       vol. 6, pp. 163–172, June 2003.
- 724 [15] D. Pereira, J. Fernandes, and P. Belanger, “Ex Vivo Assessment of Cor-  
725       tical Bone Properties Using Low-Frequency Ultrasonic Guided Waves,”  
726       *IEEE Transactions on Ultrasonics, Ferroelectrics, and Frequency Con-*  
727       *trol*, vol. 67, pp. 910–922, May 2020.
- 728 [16] N. Bochud, Q. Vallet, Y. Bala, H. Follet, J.-G. Minonzio, and P. Laugier,  
729       “Genetic algorithms-based inversion of multimode guided waves for cor-  
730       tical bone characterization,” *Physics in Medicine and Biology*, vol. 61,  
731       pp. 6953–6974, Oct. 2016.
- 732 [17] G. Haiat, S. Naili, M. Ba Vu, C. Desceliers, and C. Soize, “Equivalent  
733       contributing depth investigated by a lateral wave with axial transmission  
734       in viscoelastic cortical bone,” *The Journal of the Acoustical Society of*  
735       *America*, vol. 129, pp. EL114–EL120, Apr. 2011.
- 736 [18] J. Foiret, J.-G. Minonzio, C. Chappard, M. Talmant, and P. Laugier,  
737       “Combined estimation of thickness and velocities using ultrasound  
738       guided waves: a pioneering study on in vitro cortical bone samples,”  
739       *IEEE Transactions on Ultrasonics, Ferroelectrics, and Frequency Con-*  
740       *trol*, vol. 61, pp. 1478–1488, Sept. 2014.

- 741 [19] J.-G. Minonzio, J. Foiret, P. Moilanen, J. Pirhonen, Z. Zhao, M. Tal-  
742 mant, J. Timonen, and P. Laugier, “A free plate model can predict  
743 guided modes propagating in tubular bone-mimicking phantoms,” *The*  
744 *Journal of the Acoustical Society of America*, vol. 137, pp. EL98–EL104,  
745 Jan. 2015.
- 746 [20] S. Naili, M.-B. Vu, Q. Grimal, M. Talmant, C. Desceliers, C. Soize, and  
747 G. Haïat, “Influence of viscoelastic and viscous absorption on ultrasonic  
748 wave propagation in cortical bone: Application to axial transmission,”  
749 *The Journal of the Acoustical Society of America*, vol. 127, pp. 2622–  
750 2634, Apr. 2010.
- 751 [21] P. Moilanen, M. Talmant, V. Kilappa, P. Nicholson, S. Cheng, J. Timo-  
752 nen, and P. Laugier, “Modeling the impact of soft tissue on axial trans-  
753 mission measurements of ultrasonic guided waves in human radius,” *The*  
754 *Journal of the Acoustical Society of America*, vol. 124, pp. 2364–2373,  
755 Oct. 2008.
- 756 [22] T. N. Tran, L. Stieglitz, Y. J. Gu, and L. H. Le, “Analysis of Ultra-  
757 sonic Waves Propagating in a Bone Plate over a Water Half-Space with  
758 and without Overlying Soft Tissue,” *Ultrasound in Medicine & Biology*,  
759 vol. 39, pp. 2422–2430, Dec. 2013.
- 760 [23] Y. Li, K. Xu, Y. Li, F. Xu, D. Ta, and W. Wang, “Deep Learning  
761 Analysis of Ultrasonic Guided Waves for Cortical Bone Characteriza-  
762 tion,” *IEEE Transactions on Ultrasonics, Ferroelectrics, and Frequency*  
763 *Control*, vol. 68, no. 4, pp. 935–951, 2021.

- 764 [24] R. M. Zebaze, A. Ghasem-Zadeh, A. Bohte, S. Iuliano-Burns, M. Mi-  
765 rams, R. I. Price, E. J. Mackie, and E. Seeman, “Intracortical remod-  
766 elling and porosity in the distal radius and post-mortem femurs of  
767 women: a cross-sectional study,” *The Lancet*, vol. 375, pp. 1729–1736,  
768 May 2010.
- 769 [25] P. Moilanen, “Ultrasonic guided waves in bone,” *IEEE Transactions on*  
770 *Ultrasonics, Ferroelectrics and Frequency Control*, vol. 55, pp. 1277–  
771 1286, June 2008.
- 772 [26] D. Ta, W. Wang, Y. Wang, L. H. Le, and Y. Zhou, “Measurement of  
773 the Dispersion and Attenuation of Cylindrical Ultrasonic Guided Waves  
774 in Long Bone,” *Ultrasound in Medicine & Biology*, vol. 35, pp. 641–652,  
775 Apr. 2009.
- 776 [27] A. Chaboty, V.-H. Nguyen, G. Haiat, and P. Bélanger, “Cortical bone  
777 plate properties assessment using inversion of axially transmitted low  
778 frequency ultrasonic guided waves,” *The Journal of the Acoustical Soci-  
779 ety of America*, vol. 156, pp. 954–967, Aug. 2024.
- 780 [28] F. Seyfaddini, H. Nguyen-Xuan, and V.-H. Nguyen, “Wave disper-  
781 sion analysis of three-dimensional vibroacoustic waveguides with semi-  
782 analytical isogeometric method,” *Computer Methods in Applied Mechan-  
783 ics and Engineering*, vol. 385, p. 114043, Nov. 2021.
- 784 [29] F. Seyfaddini, H. Nguyen-Xuan, and V.-H. Nguyen, “A semi-analytical  
785 isogeometric analysis for wave dispersion in functionally graded plates  
786 immersed in fluids,” *Acta Mechanica*, vol. 232, pp. 15–32, Jan. 2021.

- 787 [30] Z. A. B. Ahmad, J. M. Vivar-Perez, and U. Gabbert, “Semi-analytical  
788 finite element method for modeling of lamb wave propagation,” *CEAS*  
789 *Aeronautical Journal*, vol. 4, pp. 21–33, Apr. 2013.
- 790 [31] J. Wu and F. Cubberley, “Measurement of velocity and attenuation of  
791 shear waves in bovine compact bone using ultrasonic spectroscopy,” *Ul-*  
792 *trasound in Medicine & Biology*, vol. 23, pp. 129–134, Jan. 1997.
- 793 [32] M. Sasso, G. Haiat, Y. Yamato, S. Naili, and M. Matsukawa, “Depen-  
794 dence of ultrasonic attenuation on bone mass and microstructure in  
795 bovine cortical bone,” *Journal of Biomechanics*, vol. 41, pp. 347–355,  
796 Jan. 2008.
- 797 [33] D. Royer and E. Dieulesaint, *Elastic Waves in Solids I: Free and Guided*  
798 *Propagation*. Springer Science & Business Media, Nov. 1999. Google-  
799 Books-ID: SzwQ1UYspyQC.
- 800 [34] T. D. Mast, “Empirical relationships between acoustic parameters in  
801 human soft tissues,” *Acoustics Research Letters Online*, vol. 1, pp. 37–  
802 42, Oct. 2000.
- 803 [35] B. Alouache, D. Laux, A. Hamitouche, K. Bachari, and T. Boutkedjirt,  
804 “Ultrasonic characterization of edible oils using a generalized fractional  
805 model,” *Applied Acoustics*, vol. 131, pp. 70–78, Feb. 2018.
- 806 [36] R. Chanamai and D. J. McClements, “Ultrasonic attenuation of edible  
807 oils,” *Journal of the American Oil Chemists’ Society*, vol. 75, pp. 1447–  
808 1448, Oct. 1998.

- 809 [37] J. Yan, W. M. Wright, J. A. O'Mahony, Y. Roos, E. Cuijpers, and S. M.  
810 Van Ruth, "A sound approach: Exploring a rapid and non-destructive  
811 ultrasonic pulse echo system for vegetable oils characterization," *Food*  
812 *Research International*, vol. 125, p. 108552, Nov. 2019.
- 813 [38] W. Karunasena, A. H. Shah, and S. K. Datta, "Wave Propagation in a  
814 Multilayered Laminated Cross-Ply Composite Plate," *Journal of Applied*  
815 *Mechanics*, vol. 58, pp. 1028–1032, Dec. 1991.
- 816 [39] M. V. Predoi, M. Castaings, B. Hosten, and C. Bacon, "Wave propaga-  
817 tion along transversely periodic structures," *The Journal of the Acous-*  
818 *tical Society of America*, vol. 121, pp. 1935–1944, Apr. 2007.
- 819 [40] M.-B. Vu and T. Nguyen-Sy, "On the effective anisotropic elastic proper-  
820 ties of porous hydroxyapatite, porous collagen, and cortical bone: A ho-  
821 mogenization scheme with percolation threshold concept," *Mathematics*  
822 *and Mechanics of Solids*, vol. 24, pp. 1091–1102, Apr. 2019. Publisher:  
823 SAGE Publications Ltd STM.
- 824 [41] M. Muller, D. Mitton, P. Moilanen, V. Bousson, M. Talmant, and  
825 P. Laugier, "Prediction of bone mechanical properties using QUS and  
826 pQCT: Study of the human distal radius," *Medical Engineering &*  
827 *Physics*, vol. 30, pp. 761–767, July 2008.
- 828 [42] J.-Y. Rho, L. Kuhn-Spearing, and P. Zioupos, "Mechanical properties  
829 and the hierarchical structure of bone," *Medical Engineering & Physics*,  
830 vol. 20, pp. 92–102, Mar. 1998.

- 831 [43] V. Sansalone, S. Naili, V. Bousson, C. Bergot, F. Peyrin, J. Zarka, J. D.  
832 Laredo, and G. Haïat, “Determination of the heterogeneous anisotropic  
833 elastic properties of human femoral bone: From nanoscopic to organ  
834 scale,” *Journal of Biomechanics*, vol. 43, pp. 1857–1863, July 2010.
- 835 [44] D. Alleyne and P. Cawley, “A two-dimensional Fourier transform method  
836 for the measurement of propagating multimode signals,” *The Journal of  
837 the Acoustical Society of America*, vol. 89, pp. 1159–1168, Mar. 1991.
- 838 [45] M. O. Culjat, D. Goldenberg, P. Tewari, and R. S. Singh, “A Review of  
839 Tissue Substitutes for Ultrasound Imaging,” *Ultrasound in Medicine &  
840 Biology*, vol. 36, pp. 861–873, June 2010.
- 841 [46] J.-G. Minonzio, M. Talmant, and P. Laugier, “Guided wave phase ve-  
842 locity measurement using multi-emitter and multi-receiver arrays in the  
843 axial transmission configuration,” *The Journal of the Acoustical Society  
844 of America*, vol. 127, pp. 2913–2919, May 2010.
- 845 [47] N. Bochud, Q. Vallet, J.-G. Minonzio, and P. Laugier, “Predicting  
846 bone strength with ultrasonic guided waves,” *Scientific Reports*, vol. 7,  
847 p. 43628, Mar. 2017.
- 848 [48] J.-G. Minonzio, N. Bochud, Q. Vallet, Y. Bala, D. Ramiandrisoa, H. Fol-  
849 let, D. Mitton, and P. Laugier, “Bone cortical thickness and porosity as-  
850 sessment using ultrasound guided waves: An ex vivo validation study,”  
851 *Bone*, vol. 116, pp. 111–119, Nov. 2018.
- 852 [49] B. Pavlakovic, M. Lowe, D. Alleyne, and P. Cawley, “Disperse: A Gen-  
853 eral Purpose Program for Creating Dispersion Curves,” in *Review of*

- 854 *Progress in Quantitative Nondestructive Evaluation* (D. O. Thompson  
855 and D. E. Chimenti, eds.), pp. 185–192, Boston, MA: Springer US, 1997.
- 856 [50] D. Pereira, G. Haiat, J. Fernandes, and P. Belanger, “Effect of intra-  
857 cortical bone properties on the phase velocity and cut-off frequency of  
858 low-frequency guided wave modes (20–85 kHz),” *The Journal of the*  
859 *Acoustical Society of America*, vol. 145, pp. 121–130, Jan. 2019.
- 860 [51] C. Desceliers, C. Soize, Q. Grimal, G. Haiat, and S. Naili, “A time-  
861 domain method to solve transient elastic wave propagation in a mul-  
862 tilayer medium with a hybrid spectral-finite element space approxima-  
863 tion,” *Wave Motion*, vol. 45, pp. 383–399, Mar. 2008.